The Cryosphere, 8, 905–913, 2014
www.the-cryosphere.net/8/905/2014/
doi:10.5194/tc-8-905-2014


The Cryosphere Open Access

# Weekly gridded Aquarius L-band radiometer/scatterometer observations and salinity retrievals over the polar regions – Part 1: Product description

**L. Brucker**[1,2], **E. P. Dinnat**[1,3], **and L. S. Koenig**[1]

[1]NASA GSFC, Cryospheric Sciences Laboratory, Code 615, Greenbelt, MD 20771, USA
[2]Universities Space Research Association, Goddard Earth Sciences Technology and Research Studies and Investigations, Columbia, MD 21044, USA
[3]Chapman University, School of Earth and Environmental Sciences, Orange CA, 92866, USA

*Correspondence to:* L. Brucker (ludovic.brucker@nasa.gov)

Received: 25 November 2013 – Published in The Cryosphere Discuss.: 12 December 2013
Revised: 6 March 2014 – Accepted: 23 March 2014 – Published: 16 May 2014

**Abstract.** Passive and active observations at L band (frequency ∼ 1.4 GHz) from the Aquarius/SAC-D mission offer new capabilities to study the polar regions. Due to the lack of polar-gridded products, however, applications over the cryosphere have been limited. We present three weekly polar-gridded products of Aquarius data to improve our understanding of L-band observations of ice sheets, sea ice, permafrost, and the polar oceans. Additionally, these products intend to facilitate access to L-band data, and can be used to assist in algorithm developments. Aquarius data at latitudes higher than 50° are averaged and gridded into weekly products of brightness temperature (TB), normalized radar cross section (NRCS), and sea surface salinity (SSS). Each grid cell also contains sea ice fraction, the standard deviation of TB, NRCS, and SSS, and the number of footprint observations collected during the seven-day cycle. The largest 3 dB footprint dimensions are 97 km × 156 km and 74 km × 122 km (along × across track) for the radiometers and scatterometer, respectively. The data is gridded to the Equal-Area Scalable Earth version 2.0 (EASE2.0) grid, with a grid cell resolution of 36 km. The data sets start in August 2011, with the first Aquarius observations and will be updated on a monthly basis following the release schedule of the Aquarius Level 2 data sets. The weekly gridded products are distributed by the US National Snow and Ice Data Center at http://nsidc.org/data/aquarius/index.html.

## 1 Introduction

The cryosphere has been extensively studied using passive microwave satellite observations for over four decades. The first imaging radiometer, the electrically scanning microwave radiometer, launched in 1972 provided the earliest maps of the global sea ice cover (Zwally et al., 1983). In 1978, the longest continuous passive microwave data record started with the launch of the scanning multichannel microwave radiometer (SMMR). This data record continues to the present with the series of special sensor microwave imager sounder (SSM/I, SSMIS), and advanced microwave scanning radiometers (AMSR-E, AMSR2), and is used extensively to monitor sea ice cover properties, ice sheet melt, and seasonal snow on land. The lowest frequency observations available from this long-term record are at ∼ 7 GHz with SMMR and the AMSRs, and at 18 GHz with the SSM/Is.

Some of the earliest passive L-band (∼ 1.4 GHz) observations of Earth occurred in the 1970s when the Skylab S-194 radiometer collected low-latitude observations (Jackson et al., 2004). The orbit characteristics of Skylab S-194 did not enable the monitoring of the polar regions. Routine passive L-band monitoring of the polar regions started much later, in 2009, with passive L-band observations from the European Space Agency's Soil Moisture and Ocean Salinity (SMOS) mission. SMOS was followed by the Aquarius/SAC-D mission in August 2011 that provides both passive and active L-band observations. L-band observations will continue in the

future with the Soil Moisture Active/Passive (SMAP) mission (launch currently planned for late 2014).

Active L-band sensors have a longer presence in space than passive L-band sensors. The Japanese Earth Resources Satellite 1 (JERS-1) operated an L-band (HH polarization) synthetic aperture radar (SAR) between 1992 and 1998. It was followed by an improved system, the phased array type L-band synthetic aperture radar (PALSAR), that operated onboard Advanced Land Observing Satellite (ALOS) from 2006 to 2011. For the near future, a PALSAR follow-on mission is planned for launch in 2014. In August 2011, Aquarius added to the active L-band instruments the first space-borne L-band scatterometer.

Despite the fact that these passive and active missions were primarily designed for the monitoring of either sea surface salinity (SSS), soil moisture, or cartography, new applications are being developed to study the cryosphere. In the microwave domain, dry snow and ice are low-loss media and the radiation penetrates into the snow/ice cover. Penetration of microwaves is inversely proportional to losses due to scattering and absorption, and thus increases as frequency decreases. L-band dry snow and ice dielectric losses are very small (e.g., Mätzler, 1987; Warren et al., 2008), and the L-band radiation may emanate from one to two orders of magnitude deeper than the radiation observed at 6.9 GHz (Surdyk, 2002). Moreover, penetration depth increases as the incidence angle decreases. Thus, the L-band radiation observed by Aquarius sensors, with relatively low-incidence angles down to $\sim 29°$, can emanate from hundreds to thousands of meters deep (i.e., centuries old ice over the Antarctic plateau).

The uniqueness of L-band emission over the polar regions, highlighted by its large penetration depth, opens new research topics. Over the ice sheets, L-band observations motivate the development of innovative approaches to study long-term climatic changes. Moreover, specific regions of the Antarctic ice sheet can be used as calibration and validation sites for L-band radiometers (e.g., Drinkwater et al., 2004; Macelloni et al., 2013). Over sea ice, investigations show that L-band radiometric observations contain information about sea ice thickness (e.g., Kaleschke et al., 2010), and over land the soil freeze/thaw state can be determined in sub-Arctic environments (e.g., Rautiainen et al., 2012).

Aquarius data are distributed by NASA's Physical Oceanography Distributed Active Archive Center (PO.DAAC). The Aquarius Level 2 product consists of the observations and retrievals along the swath. The Aquarius Level 3 products are 1° gridded SSS, averaged over different timescales, for example, daily, weekly, monthly, and seasonal timescales (Wentz and Le Vine, 2012; Le Vine et al., 2012). The Aquarius products available do not include gridded data sets of brightness temperature (TB) and normalized radar cross section (NRCS), and the Level 3 SSS products use a projection that is not optimal for studying the high latitudes.

To allow for an efficient use of the Aquarius data over the polar regions, and to move forward our understanding of the L-band observations of ice sheet, sea ice, permafrost, and polar oceans, we present in this paper three weekly polar-gridded products of TB, NRCS, and SSS. These products also include sea ice fraction. According to the orbit and sensor characteristics, the temporal resolution of the product was set to one week, corresponding to the time of revisit. Since the Aquarius' sensors are in a push-broom alignment, weekly gridded product provides the largest spatial coverage. The gridded products were produced on the Equal-Area Scalable Earth version 2.0 (EASE2.0) grid (Brodzik et al., 2012). Each grid cell is 36 km × 36 km. This grid and resolution were selected because they offer a fair compromise between high sampling along track (an observation every 10 km) and the distance between Aquarius tracks, and they will be used by SMAP.

We describe the Aquarius radiometers and scatterometer in Sects. 2.1 and 2.2, respectively. In Sect, 2.3, we introduce their observations and the criteria for valid data. In Sect. 3, we present the details of the Aquarius weekly polar-gridded products. They are distributed by the US National Snow and Ice Data Center (NSIDC) at http://nsidc.org/data/aquarius/index.html; they cover the entire Aquarius mission period since its start in August 2011. It is anticipated that the products will be updated on a monthly basis following the release schedule of the Level 2 data sets by PO.DAAC. The companion paper by Brucker et al. (2014a) focuses on the description of the Aquarius observations and retrievals over the Greenland and Antarctic ice sheets, sea ice in both hemispheres, and polar oceans.

## 2 Aquarius sensors

The Aquarius/SAC-D mission was developed collaboratively between the US National Aeronautics and Space Administration (NASA) and the Argentinian's space agency, Comisión Nacional de Actividades Espaciales (CONAE). The mission was primarily designed to monitor SSS using a combination of passive and active microwave observations.

Aquarius has one fixed dish, and it operates three L-band radiometers at three incidence angles, each providing a TB at 1.413 GHz. The radiometers have one feed horn each, and they operate independently, with different electronic systems (hereinafter referred to as radiometer 1, 2, or 3 depending on the incidence angle).

Aquarius also has one scatterometer providing a NRCS at 1.26 GHz (Yueh et al., 2012a). The one scatterometer uses the same three feed horns as the radiometers, and its observations are thus coincident with the radiometers' observations. Hereinafter, we refer to NRCS observations from beam 1, beam 2, and beam 3 depending on the incidence angle. A finer description of the sensors is provided in Sects. 2.1 and 2.2.

### 2.1 Aquarius radiometers

The Aquarius passive instruments consist of three radiometers at three incidence angles, each providing TB at 1.413 GHz. The three radiometers (1, 2, and 3, as the incidence angle increases 29.2°, 38.4°, and 46.3°, respectively) are in a push-broom alignment (i.e., non-scanning) pointing to the right-hand side of the orbit. During the ascending pass, Aquarius crosses the equatorial node at 18:00 LT (local time). Most of the time, the radiometers point to the night side of the sun-synchronous orbit, but solar contamination in the main beams is possible at high latitudes seasonally (Dinnat and Le Vine, 2008). The Aquarius incidence angles are low in comparison with other radiometers used to study the cryosphere, which typically operate at incidence angles of 53–55°, closer to the Brewster angle for the snow–air interface. The lower Aquarius incidence angles imply that observations are more sensitive to the snow–air interface, and surface snow metamorphism (Brucker et al., 2014b).

Table 1 provides the radiometers' footprint dimensions, which are increasing as the incidence angle increases. The spacecraft orbits with a seven-day repeat cycle. These characteristics, and the fact that the radiometers are in a push-broom alignment, imply that the spatial coverage becomes sparser as latitude decreases. According to the orbit inclination and the different radiometers' incidence angles, the areas unobserved at the poles differ for each sensor and hemisphere (Table 1). In the Northern Hemisphere, the largest coverage is obtained using beam 3, whereas in the Southern Hemisphere beam 3 has the smallest coverage.

While Aquarius observations are recorded in a large footprint (from 94 km × 76 km to 156 km × 97 km, as incidence angle increases), its observations are acquired with a fine sensitivity (noise equivalent differential temperature, $\mathrm{NE}\Delta T$) of $\sim 0.15$ K (Le Vine et al., 2010) per 1.44 s observation sample over the ocean. Observations have shown stability within $\pm 0.2$ K over the ocean and celestial sky over several months (Dinnat et al., 2013; Lagerloef et al., 2013). In comparison, SMOS has a finer spatial resolution that depends on the viewing angle and the data processing. The 3 dB half power beam width of SMOS corresponds to a 43 km footprint on average over the field of view, but ranges between 30 km × 30 km to 90 km × 33 km depending on the incidence angle (Kerr et al., 2010). SMOS observations, however, have lower sensitivity: over two weeks, it is 2.0 K at boresight and 2.5 K at 32° off boresight, which is the edge of the field of view (table 2 in Martin-Neira et al., 2010). The sensitivity of SMOS will be larger over a shorter time period (e.g., for one snapshot). The forthcoming SMAP mission is designed with an accuracy of 1.3 K and a 3 dB footprint of approximately 40 km (Entekhabi et al., 2010), placing it between SMOS and Aquarius in spatial resolution and accuracy.

Aquarius TB are observed in vertical (V) and horizontal (H) polarizations. The third Stokes parameter ($U$) is also measured. At L band, $U$ emitted by the ocean surface is small, and the assumption of $U = 0$ is used in the Aquarius Level 2 processing to retrieve properties of the Faraday rotation in the ionosphere (Yueh, 2000), and properties of the antenna cross-polarization coupling (Le Vine et al., 2011b; Kim et al., 2011). As shown by Yueh et al. (2013), there could be a sizeable variation of $U$ over the oceans for large wind speeds, but a study of the ice-covered surfaces is still to be carried out. Analysis of $U$ at higher frequencies with WindSat (e.g., 10.7 or 37 GHz) have shown that over the Antarctic ice sheet there is a small dependency on the azimuth angle (Narvekar et al., 2010). Over sea ice, WindSat $U$ observations were low except during the melt season, and in the marginal ice zone (Narvekar et al., 2011).

### 2.2 Aquarius scatterometer

Aquarius' active instrument consists of one scatterometer observing NRCS at 1.26 GHz. The Aquarius scatterometer does not operate at the same frequency as the three radiometers because the frequency band (1.400–1.427 GHz) is protected for passive sensors on Earth exploration satellites and radio astronomy space research (International Telecommunication Union, 2012). Moreover, operating the scatterometer at a slightly lower frequency protects the radiometers from direct contaminations. Aquarius' scatterometer uses the same three feed horns as the radiometers, providing NRCS observations at the same incidence angles as the TB observations (Table 2). The footprint sizes are slightly smaller due to the two-way path from the spacecraft to the surface and back, despite the lower frequency. Scatterometer's sensitivity varies with incidence angle (Table 2), and the calibration stability is within 0.1 dB (Yueh et al., 2012b).

For all practical purposes, the radiometer and scatterometer measurements are considered coincident. The data used to produce the weekly gridded products are from the Level 2 product, which consists of 1.44 s observation samples. These blocks are composed of twelve 120 ms subsamples, during which the radiometers and scatterometer measure alternatively over 10 ms samples. During this time sample, the footprint moves only a few meters on the ground (an infinitesimal fraction of the footprint size) and environmental parameters are considered constant.

NRCS are observed at four polarizations: VV, VH, HV, and HH. Despite the fact that antenna NRCS are measured at the four polarizations, the NRCS at the two cross polarizations are assumed identical at the top of the atmosphere. Any differences at the antenna is assumed to be due to Faraday rotation, and antenna cross-polarization coupling. Therefore, only NRCS from one cross-polarization channel is considered in this product.

### 2.3 Aquarius observations

Both passive and active L-band observations are impacted by radio frequency interference (RFI). Although L-band

**Table 1.** Characteristics of the Aquarius L-band radiometers.

| Radiometer | 1 | 2 | 3 |
|---|---|---|---|
| Incidence angle (°) | 29.2 | 38.4 | 46.3 |
| 3 dB footprint size along × across track (km × km) | 76 × 94 | 84 × 120 | 97 × 156 |
| Northernmost latitude monitored (° N) | 84.99 | 86.07 | 87.40 |
| Southernmost latitude monitored (° S) | 79.01 | 77.90 | 76.54 |

**Table 2.** Beam-dependent characteristics of the Aquarius L-band scatterometer.

| Beam | 1 | 2 | 3 |
|---|---|---|---|
| 3 dB two-way footprint size along × across track (km × km) | 58 × 71 | 65 × 91 | 74 × 122 |
| NE $\sigma^0$ (dB) | −29 | −26 | −24 |
| Scatterometer sensitivity (dB) | 0.04 | 0.06 | 0.1 |
| Scatterometer stability for 7 days (dB) | 0.13 | 0.13 | 0.13 |

missions operate their radiometers in a protected spectral band, RFI is an issue, especially in the Northern Hemisphere. Aquarius has a high-radiometric sensitivity and short-time sampling that enhance detection of low-level RFI. The detection of RFI in the Aquarius radiometer observation is based on the algorithm of Misra and Ruf (2008), which identifies individual samples of the antenna temperature that deviate significantly from the average value of nearby samples over a very brief temporal window (ms). Mitigation is accomplished in subsequent processing steps by excluding contaminated samples before averaging all presumed RFI-free observations within a 1.44 s samples which is then converted to antenna temperatures. The RFI detection algorithm is applied independently to each radiometer channel. See sect. 7 of Piepmeier et al. (2013) for further detailed information. The detection and mitigation of RFI in the Aquarius scatterometer observation are based on two methods described in sect. 8 of Yueh et al. (2012a). One method is based on a sensitive on-board RFI flagging technique, and the other is a ground-based, outlier flagging method.

In the weekly gridded products presented in Sect. 3, every data associated with an RFI flag in the Level 2 products is eliminated. Figure 1 presents an example of weekly RFI occurrence in the Northern Hemisphere. RFI contamination is persistent over northern and eastern Europe, and along the north warning system (NWS) at a latitude of $\sim 70°$ N in North America. The RFI resulting from the NWS impacts Aquarius observations in different regions and with a different intensity whether the spacecraft is in an ascending or descending orbit. Of note, for polar studies there is RFI contamination over Greenland only during descending orbits when Aquarius sensors are pointing toward the NWS line (Fig. 1, right). In the high latitudes of the Southern Hemisphere L-band RFI occurrences are rare ($\sim 30$ instances in 2013), and contamination was never repeated in a given grid cell (Fig. 2).

To develop the Aquarius weekly polar-gridded products for latitudes higher than 50°, we only used information from the Level 2 product (Wentz and Le Vine, 2012). The Aquarius Level 2 product (version 2.8, March 2014) consists of the footprint observations and retrievals along track (swath data). It also consists of ancillary data, flags, converted telemetry, and navigation data. One example of ancillary data is the sea ice fraction (ICEF). The ICEF results from a combination of two elements: estimated sea ice concentration, and antenna characteristics. Sea ice concentration estimates are obtained from the analysis by NOAA's Marine Modeling and Analysis Branch (http://polar.ncep.noaa.gov/seaice/Analyses.shtml), available daily at a spatial resolution of 1/12°, and distributed by the US National Centers for Environmental Prediction (NCEP) as the Global Forecast System (GFS) Global Data Assimilation System (GDAS) sea ice product. Hereinafter, the use of ICEF refers to the estimated sea ice concentration integrated over the sensor's field of view and weighted by the antenna gain patterns. Similarly, land fraction data is integrated over the sensor's field of view and weighted by the antenna gain patterns (Dinnat and Le Vine, 2007; Le Vine et al., 2011b).

The Level 2 TB product is computed after empirical calibration of the measured antenna temperatures against a forward radiative transfer model over ocean surfaces (Le Vine et al., 2011a). More details about the Level 2 processing can be found in Wentz and Le Vine (2012), Le Vine et al. (2012), and Piepmeier et al. (2013). Briefly, the antenna temperatures are corrected for

- the emission of extraterrestrial sources (Sun, Moon, celestial sky), that reaches directly the antenna through the side and back lobes;
- the effect of the integration over the antenna gain patterns;
- the Faraday rotation;

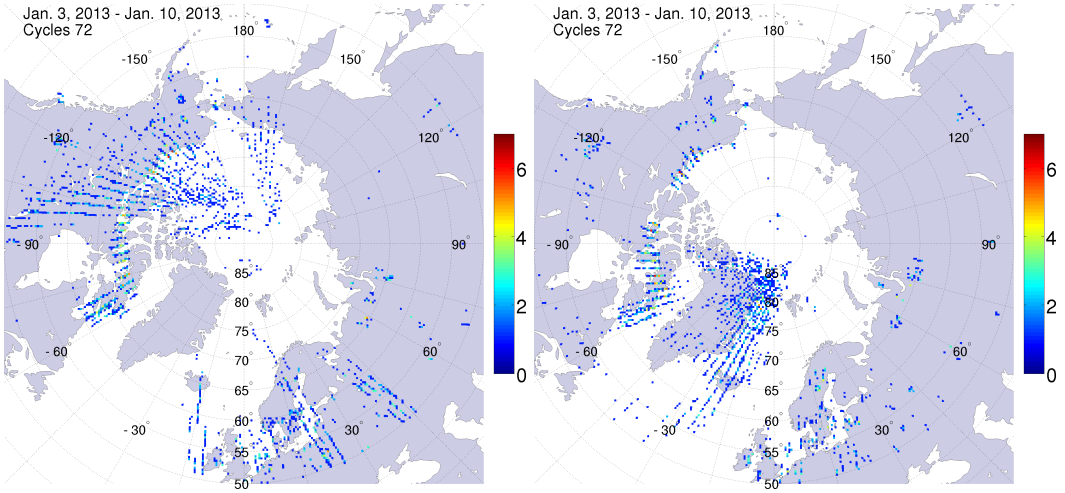


**Fig. 1.** Map of radio frequency interference (RFI) occurrences (the number of footprint with either a moderate or severe RFI contamination) during cycle 72 (3–10 January 2013) in the Northern Hemisphere for ascending (left) and descending (right) orbits.

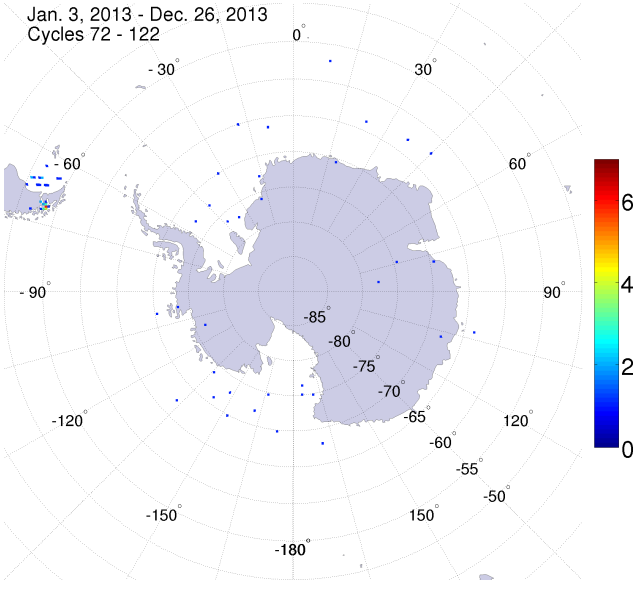


**Fig. 2.** Map of radio frequency interference (RFI) occurrences (the number of footprint with either a moderate or severe RFI contamination) during the entire year 2013 in the Southern Hemisphere, considering both ascending and descending orbits.

– atmospheric effects (upward emission, downward emission reflected at the surface, and attenuation of the signals from the surface).

These corrections provide the TBs at the Earth's surface. Over the oceans, the TB is corrected for the effects of surface roughness (including the reflected/scattered galaxy and Sun) using the scatterometer observations and a simulated wind speed. The remaining TB for a smooth surface is converted into SSS using ancillary data for the sea surface temperature, and a model for the sea water dielectric constant. Data sets provided in the weekly polar-gridded products described here do not apply corrections to the Level 2 product. We use these Aquarius Level 2 data to produce weekly gridded products of TB (at V and H polarizations), NRCS (at VV, VH, and HH polarizations), SSS, and ICEF.

## 3 Weekly polar-gridded product details

To create a gridded product the projection, spatial resolution, and temporal resolution must be specified. These characteristics were defined according to the satellite observations, and to ensure consistency with the forthcoming SMAP mission. The EASE2.0 grid (Brodzik et al., 2012) was chosen, and the grid cell spatial resolution set to 36 km × 36 km. These characteristics are appropriate for the Aquarius observations at latitudes higher than 50°. At these high latitudes, there are limited areas not observed. Therefore, the trade-off between spatial resolution and data coverage is fair. Since Aquarius observations are, however, recorded every 10 km along track, it is possible for specific applications to grid the data with a refined spatial resolution better than 36 km. According to the orbit and sensor characteristics, the temporal resolution of the product was set to one week, corresponding to the time of revisit. Since the Aquarius' sensors are in a push-broom alignment, a weekly gridded product provides the largest spatial coverage.

Gridded data were produced using all the Aquarius observations flagged as RFI free, and recorded during nominal operation of the spacecraft. Non-nominal operation dates include maneuvers and anomaly periods; they are reported on the Aquarius status web page (http://oceancolor.gsfc.nasa.gov/sdpscgi/public/aquarius_report.cgi).

For TB, each radiometer was treated independently to produce three weekly gridded TB products corresponding to observations from the ascending orbit, the descending orbit, and both orbit types combined. In addition, the distinction per radiometer is necessary due to the different incidence angles, which lead to different reflection intensities at the interface created by dielectric constant changes (e.g., at the snow–air interface). For each seven-day cycle, all observations from a given radiometer (meeting the above criteria) whose footprint center was within a given 36 km grid cell were averaged together, and the standard deviation was calculated. For each week and hemisphere, eighteen TB maps are produced and distributed (one for each of the three radiometers, each of the two polarizations, and each of the three orbit combinations).

For NRCS, each beam and each orbit type was treated independently. The distinction for each beam is also needed due to the different incidence angles. The distinction between each orbit type is necessary because of the anisotropy of the ice-covered surfaces (Brucker et al., 2014a). For each week and hemisphere, eighteen NRCS maps are produced and distributed (one for each of the three beams, each of the three polarizations, and each of the two orbit combinations).

For SSS, two weekly gridded products are available. The first product provides the SSS corresponding to the weekly gridded TB. Data are separated per beam and per orbit type, and include combined ascending and descending orbits. The second product combines the SSS retrieved from the three beams and both orbit types using the maximum amount of retrievals.

SSS retrievals where the radiometer land fraction was $\geq 0.25$ were not considered. If left uncorrected, a land fraction of as little as 0.001 can be detrimental to the SSS retrieval ($\sim$ 0.2–0.4 psu error; Dinnat and Le Vine, 2007). However, there is a first order correction for the effect of land contamination in the Level 2 SSS retrieval that should remove most of the error (sect. 3.8 in Wentz and Le Vine, 2012). In addition, the level of acceptable residual error in coastal studies will depend on specific applications of the product. For these reasons, we set a relatively high threshold for land contamination. Because we provide the information on the mean land fraction for each grid cell, the user has the opportunity to select a more stringent threshold if needed.

TB, NRCS, and SSS weekly averages are provided in conjunction with the standard deviations of all footprint observations/retrievals within a grid cell. The significance of the standard deviation must be evaluated against the number of footprint observations in grid cell.

Grid cells without data can result from missing observations either because the cells fall in between beam tracks (permanently missing), or because all data gathered were deemed invalid for a given time period. In these situations, a Delaunay triangulation with linear interpolation was applied to the weekly gridded values to spatially interpolate TB and NRCS in grid cells without observations during the cycle. To avoid interpolating over too large a region in case of significant data loss, the interpolation was not applied (and a NaN element is provided) where six or more contiguous grid cells had no data. Note that because each product contains the number of footprint observations per grid cell, it is easy to identify interpolated values where the number of observations per grid cell is 0. This allows users to either disregard the interpolated data, or apply another interpolation method best suited for their studies. In any case, one must be cautious with the use of interpolated data, even though the Aquarius radiometer field of views are larger than the 36 km grid cell resolution.

The TB, NRCS, and SSS products are processed for every Aquarius cycle, and distributed in HDF5 format by NSIDC at http://nsidc.org/data/aq3_tb.html, http://nsidc.org/data/aq3_nrcs.html and http://nsidc.org/data/aq3_sss.html, respectively. Future release dates depend on the release of the Level 2 product, which are currently released monthly in a one month batch. We also provide ancillary files containing the grid cell center latitude and longitude, and the grid cell mean land fraction, as well as a look-up table to convert date to cycle number. Table 3 summarizes the data distributed in each of the three products.

### 3.1 Aquarius 36 km weekly polar-gridded TB, and SSS

This product containing TB, SSS, and ICEF is composed of six files per cycle: one per beam, and one per hemisphere. Each file contains the weekly gridded TB, SSS, and ICEF of the ascending orbits, descending orbits, and the two orbit types combined. The data sets consist of weekly mean TB V, TB H, and SSS, along with the standard deviations within the grid cell (TBV_STD, TBH_STD, and SSS_STD). This product also contains the radiometer ice fraction (ICEF_RAD and ICEF_RAD_STD for the mean and standard deviation, respectively). Standard deviation values are never interpolated. The data volume for all incidence angles, per week and per hemisphere, is $\sim$ 5.5 MB.

### 3.2 Aquarius 36 km weekly polar-gridded NRCS

This product containing NRCS and ICEF is composed of six files per cycle: one per beam, and one per hemisphere. Each file contains the weekly gridded data of the ascending and descending orbits. NRCS observations from ascending and descending orbits were not combined together due to the anisotropy of the ice-covered surfaces. The data consist of weekly mean NRCS at three polarizations (NRCS_VV, NRCS_VH, and NRCS_HH), along with the standard deviations within the grid cell (NRCS_VV_STD, NRCS_VH_STD, and NRCS_HH_STD). This product also contains the scatterometer ice fraction (ICEF_SCA and ICEF_SCA_STD for the mean and standard deviation, respectively). The data volume for all incidence angles, per week and per hemisphere, is $\sim$ 1.1 MB.

**Table 3.** Product names with the list of variables per beams and orbits. Acronyms are TB – brightness temperature; V – vertical polarization; H – horizontal polarization; STD – standard deviation; NFP – number of footprint observations; RAD – radiometer; SCA – scatterometer; SSS – sea surface salinity; ICEF – sea ice fraction; NRCS – normalized radar cross section; and SSS3b – sea surface salinity obtained by combining the three beams.

| | |
|---|---|
| Aquarius 36 km weekly polar-gridded brightness temperature, and sea surface salinity | |
| TBV, TBH | |
| TBV_STD, TBH_STD | Beams 1, 2, and 3 |
| NFP_RAD | Orbits ascending, descending, and combined |
| SSS, SSS_STD | |
| ICEF_RAD, ICEF_RAD_STD | |
| Aquarius 36 km weekly polar-gridded normalized radar cross section | |
| NRCS_VV, NRCS_VH, NRCS_HH | |
| NRCS_VV_STD, NRCS_VH_STD, NRCS_HH_STD | Beams 1, 2, and 3 |
| NFP_SCA | Orbits ascending, and descending |
| ICEF_SCA, ICEF_SCA_STD | |
| Aquarius 36 km weekly polar-gridded sea surface salinity 3 beams (SSS3b) | |
| SSS3b | |
| SSS3b_STD | Beams 1, 2, and 3 combined |
| NFP_SSS3b | Orbits combined |
| ICEF_SSS3b, ICEF_STD_SSS3b | |

### 3.3 Aquarius 36 km weekly polar-gridded SSS3b

This product combines SSS retrievals from all three beams, as retrievals of SSS should be independent of the radiometers and incidence angles. However, the error on SSS retrievals could vary slightly with the beam as the outer beam averages over a larger field of view and is more sensitive to surface roughness for example. This product is composed of two files per cycle: one per hemisphere. Each file contains the weekly gridded SSS of the ascending orbit, descending orbit, and the two orbit types combined, along with the standard deviation within the grid cell (SSS_STD). The data volume for all incidence angles, per week and per hemisphere, is $\sim 0.7$ MB.

The distinction between the two orbit types is required because differences have been identified (Lagerloef et al., 2013). The Aquarius Level 2 product version 3.0 has reduced the differences, though not completely eliminated them. While the origin of these differences has not been established yet, it is likely to be in part due to the reflected/scattered galaxy, and RFI contaminations. It is possible that residual RFI and sky contaminations impact the empirical calibration performed over the oceans, and therefore create biases dependent on the type of orbit. The correction for the reflected galaxy has been found insufficient, and an empirical adjustment was introduced for version 3.0. The galaxy contamination is very dependent on the type of orbit, because it is only significant when the contribution comes from a very limited region of the sky (e.g., the galactic plane). The different orientations of the beams for the ascending and descending passes, therefore, lead to different sections of the sky being seen by the reflected beam, and hence, very different contaminations. As illustrated in Fig. 1, RFI is also very sensitive to beam orientation whether the spacecraft is in ascending or descending orbit. Some regions of significant RFI contaminations over the oceans are off the east coast of North America, and the western European coast. Depending on the orbit type (ascending or descending), the antenna side lobes are pointing inland (where most of the RFI sources are located) or toward the open ocean. SSS retrievals in these regions likely have larger differences between the ascending and descending orbits.

## 4 Conclusions

Recent L-band satellite missions collect passive and active observations which offer new capabilities to study and to monitor the polar regions and the cryosphere. In this paper, we provided a technical description of the Aquarius' sensors and for three weekly averaged gridded products of TB, NRCS, and SSS. The products also contain ICEF. An initial analysis of these data is provided in the companion paper (Brucker et al., 2014a).

For each 36 km grid cell where satellite observations/retrievals are available the standard deviation of TB, NRCS, and SSS is provided along with the number of footprint observations collected during the seven-day cycle. Where less than six contiguous grid cells do not have data, a linear interpolation is applied. Interpolated values can be tracked by the users using the number of footprint observations.

According to the orbit and sensor characteristics, the temporal resolution of the product was set to one week, corresponding to the time of revisit. Since the Aquarius' sensors are in a push-broom alignment, a weekly gridded product provides the largest spatial coverage.

L-band observations are sensitive to RFI. Their presence is localized in the Northern Hemisphere, and substantially impacts the monitoring of continental land, Greenland, and the Beaufort sea. The magnitude of the RFI contribution depends on the orbit (ascending vs. descending). Over the Greenland Ice Sheet, observations collected during the ascending orbits are significantly less impacted by RFI.

The three products described in this paper start from late August 2011. It is anticipated that they will be updated on a monthly basis following the release schedule of the Level 2 data sets. They are available at http://nsidc.org/data/aquarius/index.html in HDF5 format for improving our understanding of low-microwave frequency observations, and for the development of new or refined algorithms.

*Acknowledgements.* This research was funded by the NASA Scientific Innovation Fund. We acknowledge PO.DAAC for distributing the Level 2 Aquarius data (version 2.0) and NSIDC for archiving and distributing the weekly gridded products presented in this paper. We also acknowledge A. Decharon and L. Taylor (University of Maine, School of Marine Sciences) for hosting the visualization of the weekly gridded products of brightness temperature and sea surface salinity on the Aquarius Education & Public Outreach website (http://aquarius.umaine.edu/cgi/gal_latitudes_tbv.htm and http://aquarius.umaine.edu/cgi/gal_latitudes_sss.htm, respectively). Finally, we acknowledge the reviewers for their useful suggestions.

Edited by: L. Kaleschke

## References

Brodzik, M. J., Billingsley, B., Haran, T., Raup, B., and Savoie, M. H.: EASE-Grid 2.0: Incremental but Significant Improvements for Earth-Gridded Data Sets, ISPRS Int. J. Geo-Inf., 1, 32–45, doi:10.3390/ijgi1010032, 2012.

Brucker, L., Dinnat, E. P., and Koenig, L. S.: Weekly gridded Aquarius L-band radiometer/scatterometer observations and salinity retrievals over the polar regions – Part 2: Initial product analysis, The Cryosphere, 8, 915–930, doi:10.5194/tc-8-915-2014, 2014a.

Brucker, L., Dinnat, E. P., Picard, G., and Champollion, N.: Effect of snow surface metamorphism on Aquarius L-band radiometer observations at Dome C, Antarctica, IEEE T. Geosci. Remote, in press, doi:10.1109/TGRS.2014.2312102, 2014b.

Dinnat, E. P., Le Vine, D., and Abraham, S.: Aquarius Cold Sky maneuvers: Assessing calibration bias, temporal drift, and antenna back lobes, IGARSS 2013, oral presentation, 2013.

Dinnat, E. P. and Le Vine, D. M.: Effects of the Antenna Aperture on Remote Sensing of Sea Surface Salinity at L-Band, IEEE T. Geosci. Remote, 45, 2051–2060, doi:10.1109/TGRS.2007.890807, 2007.

Dinnat, E. P. and Le Vine, D. M.: Impact of Sun Glint on Salinity Remote Sensing: An Example With the Aquarius Radiometer, IEEE T. Geosci. Remote, 46, 3137–3150, doi:10.1109/TGRS.2008.2000629, 2008.

Drinkwater, M. R., Floury, N., and Tedesco, M.: L-band ice sheet brightness temperatures at Dome C, Antarctica: spectral emission modelling, temporal stability and impact of the ionosphere., Ann. Glaciol., 39, 391–396, doi:10.3189/172756404781814014, 2004.

Entekhabi, D., Njoku, E., O'Neill, P., Kellogg, K., Crow, W., Edelstein, W., Entin, J., Goodman, S., Jackson, T., Johnson, J., Kimball, J., Piepmeier, J., Koster, R., Martin, N., McDonald, K., Moghaddam, M., Moran, S., Reichle, R., Shi, J.-C., Spencer, M., Thurman, S., Tsang, L., and Van Zyl, J.: The Soil Moisture Active Passive (SMAP) Mission, Proc. IEEE, 98, 704–716, doi:10.1109/JPROC.2010.2043918, 2010.

International Telecommunication Union: Radio Regulation, Vol. 1: Articles, Tech. rep., International Telecommunication Union, Switzerland, 2012.

Jackson, T. J., Hsu, A. Y., van de Griend, A., and Eagleman, J. R.: Skylab L-band microwave radiometer observations of soil moisture revisited, Int. J. Remote Sens., 25, 2585–2606, doi:10.1080/01431160310001647723, 2004.

Kaleschke, L., Maaß, N., Haas, C., Hendricks, S., Heygster, G., and Tonboe, R. T.: A sea-ice thickness retrieval model for 1.4 GHz radiometry and application to airborne measurements over low salinity sea-ice, The Cryosphere, 4, 583–592, doi:10.5194/tc-4-583-2010, 2010.

Kerr, Y., Waldteufel, P., Wigneron, J.-P., Delwart, S., Cabot, F., Boutin, J., Escorihuela, M.-J., Font, J., Reul, N., Gruhier, C., Juglea, S., Drinkwater, M., Hahne, A., Martin-Neira, M., and Mecklenburg, S.: The SMOS Mission: New Tool for Monitoring Key Elements ofthe Global Water Cycle, Proc. IEEE, 98, 666–687, doi:10.1109/JPROC.2010.2043032, 2010.

Kim, S.-B., Wentz, F., and Lagerloef, G. S. E.: Effects of Antenna Cross-Polarization Coupling on the Brightness Temperature Retrieval at L-Band, IEEE T. Geosci. Remote, 49, 1637–1648, doi:10.1109/TGRS.2010.2087028, 2011.

Lagerloef, G., Kao, H.-Y., Meln, O., Hacker, P., Hackert, E., Chao, Y., Hilburn, K., Meissner, T., Yueh, S., Hong, L., and Lee, T.: Aquarius Salinity Validation Analysis, Tech. rep., AQ-014-PS-0016, NASA, Pasadena, CA, USA, 2013.

Le Vine, D., Lagerloef, G. S. E., and Torrusio, S.: Aquarius and Remote Sensing of Sea Surface Salinity from Space, Proc. IEEE, 98, 688–703, doi:10.1109/JPROC.2010.2040550, 2010.

Le Vine, D., Dinnat, E., Abraham, S., De Matthaeis, P., and Wentz, F.: The Aquarius Simulator and Cold-Sky Calibration, IEEE T. Geosci Remote, 49, 3198–3210, doi:10.1109/TGRS.2011.2161481, 2011a.

Le Vine, D., Dinnat, E., Jacob, S., Abraham, S., and De Matthaeis, P.: Impact of Antenna Pattern on Measurement of the Third Stokes Parameter From Space at L-Band, IEEE T. Geosci. Remote, 49, 406–414, doi:10.1109/TGRS.2010.2051953, 2011b.

Le Vine, D., Meissner, T., Wentz, F., and Piepmeier, J.: Aquarius salinity retrieval algorithm (Version 2), addendum II to Algorithm Theoretical Basis Document (ATBD), Tech. Rep. 082912: Addendum II, RSS Technical Report, Santa Rosa, CA, USA, 2013.

Macelloni, G., Brogioni, M., Pettinato, S., Zasso, R., Crepaz, A., Zaccaria, J., Padovan, B., and Drinkwater, M.: Ground-Based L-Band Emission Measurements at Dome-C Antarctica: The DOMEX-2 Experiment, IEEE T. Geosci. Remote, 51, 4718–4730, 2013.

Martin-Neira, M., Corbella, I., Torres, F., Cabot, F., Closa, J., Kainulainen, J., Castro, R., Barbosa, J., Gutierrez, A., Martin-Porqueras, F., Oliva, R., Anterrieu, E., Brown, M., and McMullan, K.: SMOS payload performance assessment, in: Geoscience and Remote Sensing Symposium (IGARSS), 2010 IEEE International, 3150–3153, doi:10.1109/IGARSS.2010.5649704, 2010.

Mätzler, C.: Applications of the interaction of microwaves with the natural snow cover, Remote Sensing Reviews, 2, 259–387, 1987.

Misra, S. and Ruf, C.: Detection of Radio-Frequency Interference for the Aquarius Radiometer, IEEE T. Geosci. Remote, 46, 3123–3128, doi:10.1109/TGRS.2008.920371, 2008.

Narvekar, P., Heygster, G., Jackson, T., Bindlish, R., Macelloni, G., and Notholt, J.: Passive Polarimetric Microwave Signatures Observed Over Antarctica, IEEE T. Geosci. Remote, 48, 1059–1075, doi:10.1109/TGRS.2009.2032295, 2010.

Narvekar, P., Heygster, G., Tonboe, R., and Jackson, T.: Analysis of WindSat Third and Fourth Stokes Components Over Arctic Sea Ice, IEEE T. Geosci. Remote, 49, 1627–1636, doi:10.1109/TGRS.2010.2089058, 2011.

Piepmeier, J., Bindlish, R., Brown, S., Dinnat, E., Gales, J., Hong, L., Jackson, T., Lagerloef, G., Le Vine, D., de Matthaeis, P., Meissner, T., and C., R.: Aquarius radiometer post-launch calibration for product version 2, AQ-014-PS-0015, Tech. Rep. AQ-014-PS-0015, NASA and CONAE, Pasadena, CA, USA, 2013.

Rautiainen, K., Lemmetyinen, J., Pulliainen, J., Vehvilainen, J., Drusch, M., Kontu, A., Kainulainen, J., and Seppanen, J.: L-Band Radiometer Observations of Soil Processes in Boreal and Subarctic Environments, IEEE T. Geosci. Remote, 50, 1483–1497, doi:10.1109/TGRS.2011.2167755, 2012.

Surdyk, S.: Using microwave brightness temperature to detect short-term surface air temperature changes in Antarctica: An analytical approach, Remote Sens. Environ., 80, 256–271, 2002.

Warren, S. G. and Brandt, R. E.: Optical constants of ice from the ultraviolet to the microwave: a revised compilation, J. Geophys. Res., 113, D14220, doi:10.1029/2007JD009744, 2008.

Wentz, F. and Le Vine, D.: Aquarius salinity retrieval algorithm (Version 2) Algorithm Theoretical Basis Document (ATBD), RSS Technical Report 082912, NASA AQ-014-PS-0017, Pasadena, CA, USA, 2012.

Yueh, S.: Estimates of Faraday rotation with passive microwave polarimetry for microwave remote sensing of Earth surfaces, IEEE T. Geosci. Remote, 38, 2434–2438, doi:10.1109/36.868900, 2000.

Yueh, S., Fore, A., Freedman, A., Chaubell, M. J., Tang, W., and Neumann, G.: Aquarius Scatterometer Algorithm Theoretical Basis Document, Version 1, AQ-014-PS-0019, Tech. Rep. AQ-014-PS-0019, NASA and CONAE, Pasadena, CA, USA, 2012a.

Yueh, S., Lagerloef, G., Kao, H.-Y., Carey, D., Le Vine, D., Piepmeier, J., Dinnat, E. P., de Matthaeis, P., Hong, L., Utku, C., Ruf, C., Chen, D., Vandemark, D., Jones, L., Hejazin, Y., Brown, S., Misra, S., Neumann, G., Freedman, A., Fore, A., Tang, W., Xu , X., Bindlish, R., Hacker, P., Chao, Y., Wentz, F., Hilburn, K., Meissner, T., and Scott, J.: Aquarius Satellite Salinity Measurements, Aquarius/SACD Science Team Meeting, Buenos Aires, Tech. rep., NASA, 2012b.

Yueh, S., Tang, W., Fore, A., Neumann, G., Hayashi, A., Freedman, A., Chaubell, J., and Lagerloef, G.: L-Band Passive and Active Microwave Geophysical Model Functions of Ocean Surface Winds and Applications to Aquarius Retrieval, IEEE T. Geosci. Remote, 51, 4619–4632, doi:10.1109/TGRS.2013.2266915, 2013.

Zwally, H. J., Parkinson, C. L., and Comiso, J. C.: Variability of Antarctic Sea Ice and Changes in Carbon Dioxide, Science, 220, 1005–1012, doi:10.1126/science.220.4601.1005, 1983.